


Article

# Experimental and Numerical Studies on the Ultimate Bending Strength of Welded Plated Grillage with Combined Openings

Chen Chen <sup>\*</sup> , Hong Zhou <sup>\*</sup>, Zhengda Lv and Ziqiu Li

School of Naval Architecture and Ocean Engineering, Jiangsu University of Science and Technology, Zhenjiang 212100, China; 15142839625@163.com (Z.L.); 221110101119@stu.just.edu.cn (Z.L.)

<sup>\*</sup> Correspondence: 201010006@stu.just.edu.cn (C.C.); 199600001373@just.edu.cn (H.Z.)

**Abstract:** Plated grillage with combined openings was susceptible to complex failure behaviors as the main load-bearing structure of the superstructure on passenger ships subjected to deck loads. Additionally, the deformation and stresses generated during the welding of the plated grillage complicated the prediction of its failure behavior. In this case, a new partitioned inherent strain method and nonlinear finite element method were used to simulate the welding and loading process, and experiments were designed and carried out to make comparisons, unveiling the influence regulations between the failure behavior of the structure and the loading condition, the initial welding state. This research on the failure mode analysis of plated grillages could provide references for the optimization of the structural form of plated grillages and the cargo loading scheme on the deck of a real ship.

**Keywords:** combined opening plated grillage; initial welding state; ultimate bending strength; failure behavior

## 1. Introduction

Large passenger ships are usually composed of multideck plated grillage structures constructed from welded and assembled plates and sections. Differing from conventional ships, to meet the requirements of dense pipeline and cable arrangement as well as accommodation layout, the plated grillage is structured with a large span, high stiffener web height, and dense openings [1,2]. In addition, to reduce the weight, the plated grillage in the accommodation area is made of numerous thin plates, causing significant deformation during the welding process [3]. Structural specializations and welding deformations make the deformation behavior of such plated grillage structures complicated when subjected to vertical loads. Therefore, it is necessary to investigate the ultimate load-bearing capacity and deformation characteristics of welded combined opening plated grillage under deck load, taking into account the welding deformation and stress.

To investigate behaviors of the opening plate and girders, related scholars have made numerous explorations. For opening plates, Brown [4] first solved for the stress distribution around the perimeter of the opening using the conjugate load analysis method and investigated the effect of different opening shapes [5,6]. Later, with the evolution of computer hardware and the iteration of algorithms, finite element calculation methods were widely used. Shanmugam, Paik, and other scholars investigated the effects of opening shape, size, location, and loading method on the deformation behavior and ultimate load-bearing capacity with the aid of FEM, and summarized the designing equations [7–12]. As for the experiment, Saad-Eldden systematically investigated the effects of opening shape, size, reinforcement measure, cracking, and material corrosion on structural load-bearing capacity, and found that when the opening size is constant, small-size dense openings could alleviate the localized failure phenomenon occurring in large-size sparse openings [13–18].

For the structural and more complex combined opening girders, scholars mostly used finite element simulation and experimental methods to explore deformation regulations



**Citation:** Chen, C.; Zhou, H.; Lv, Z.; Li, Z. Experimental and Numerical Studies on the Ultimate Bending Strength of Welded Plated Grillage with Combined Openings. *J. Mar. Sci. Eng.* **2024**, *12*, 295. <https://doi.org/10.3390/jmse12020295>

Academic Editor: Joško Parunov

Received: 15 January 2024

Revised: 4 February 2024

Accepted: 5 February 2024

Published: 7 February 2024



**Copyright:** © 2024 by the authors. Licensee MDPI, Basel, Switzerland. This article is an open access article distributed under the terms and conditions of the Creative Commons Attribution (CC BY) license (<https://creativecommons.org/licenses/by/4.0/>).

and load-bearing characteristics. Sun et al. [19–21] used the FEM to investigate the failure modes of opening girders made of concrete under torsion, bending, and shear loads, and gave the corresponding reinforcement measures. Wang et al. [22] investigated the load-bearing capacity of steel hexagonal opening girders under vertical shear loads, revealing the deformation characteristics. As for the experiments, Zirakian et al. [23] carried out a load-bearing capacity experiment on hexagonal opening girders, compared the results with the Trahair formula [24], and gave suggestions for improvements for the formula generalization. Zhao et al. [2,25] designed an experimental device to carry out the ultimate load-bearing capacity of a ship's opening girder structure under the combination of axial and vertical loads, and suggested adding a guard plate around the opening to improve the capacity of the opening region.

For marine combined opening plated grillage, owing to the structural complexity, most investigations were still based on the finite element method. Li et al. [26] took the opening plated grillage on a ro-ro ship as a research object, and used the FEM to explore the influence regulations of the openings on the overall and local strength of the plated grillage, and provided suggestions for the optimization of the structure. Gan et al. [27] analyzed the effects of the initial defects and framing specifications on the ultimate bearing capacity of the opening plated grillage under longitudinal compression loads, combining the classical reinforced plate theory and the nonlinear finite element method. As for the experiments, Liu et al. [28,29] conducted the design of the loading device to investigate the failure behavior of the passenger ship opening plated grillage under axial compression loads, revealing the influence regulations of the initial defects, opening sizes, and some other parameters.

In the above-mentioned literature, there are relatively few experimental investigations on the ultimate load-bearing capacity of high stiffener web plated grillage with combined openings. For loading conditions, the action of the axial compression load was mainly considered, and little consideration was given to the deck bending load. In addition, regardless of the research on girders or plated grillages, most of the considerations for the initial welding state in the simulation were still based on empirical formulas, and the experiments were still dominated by corrective elimination. However, the passenger ship's plated grillage uses a large number of thin plates, which are prone to distinct deformation at the welding joint. Due to the difference in welding parameters, the deformation and residual stress values also differ greatly [30]. The use of empirical formulas to impose a homogenized initial defect does not reflect the detailed manufacturing process and is subjected to large errors. While using the inherent strain method, the deformation of the plated grillage can be accurately and efficiently predicted considering the welding parameters. Zhou et al. [31–34] used this approach to perform a deformation prediction of offshore platform blocks and gave process optimization measures. Therefore, the welding deformation and stress of the plated grillage can be predicted using the inherent strain method and used as the initial state for the simulation of the failure behavior to improve the accuracy of the numerical simulation.

In this study, the load-bearing capacity and failure behavior of combined opening plated grillage were investigated using numerical simulations combined with static experiments. An inhomogeneous inherent strain method was used to predict the initial stresses and deformations of the plated grillage, as an initial state to study the effect of the initial welding state on the failure behavior of the structure. Finally, the ultimate load-bearing capacity as well as the failure behavior were investigated via experimental methods combined with simulated results.

## 2. Specimens

To satisfy the demand for space arrangement in the theater area of the large passenger ship, a large-span combined opening plated grillage is used in conjunction with a pillar to achieve structural support. The plated grillage between the two longitudinal girders in this region was selected as the object to investigate its failure behavior under deck vertical loads.

The plated grillage was assembled and welded from longitudinal girders and stringers, transverses, and plates. The location of the plated grillage on the actual ship was shown in Figure 1. Referring to the existing research findings [28,29] and the site equipment conditions, the geometric and plate thickness scaling ratios were determined to be 1:4 and 1:2, respectively. The dimensions of the plated grillage and the parts were shown in Figure 2.

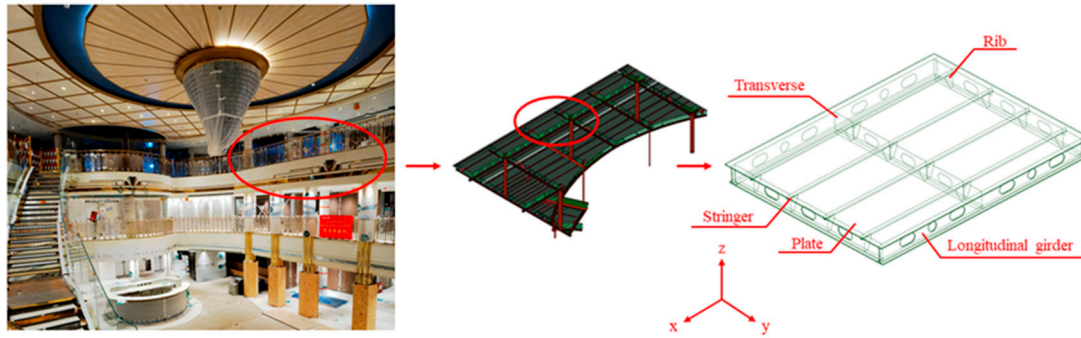


Figure 1. Schematic diagram of the plated grillage structure.

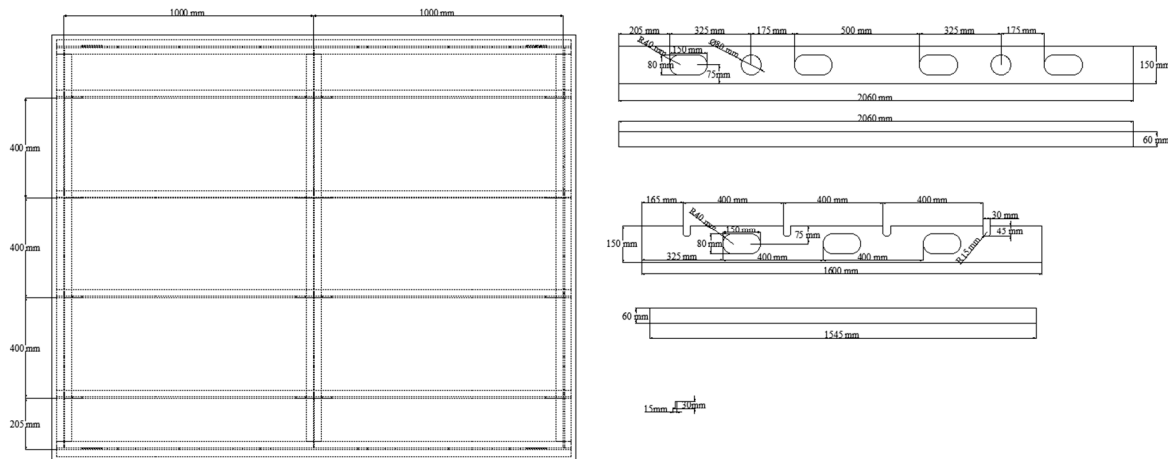


Figure 2. Diagram of the plated grillage dimensions (mm).

### 3. Simulation and Measurement of Initial Welding State

To better investigate the effect of the initial welding state in the manufacturing on the failure behavior of the structure, an inhomogeneous inherent strain method was used in this section to simulate the deformation and stress of the plated grillage concerning the actual manufacturing process. The deformation values of the measured points on the deck surface obtained from the simulation were compared with the measured values to verify the accuracy of the numerical simulation.

#### 3.1. The Actual Manufacturing Technique

The plated grillage was assembled and welded from an AH36 mild steel of 5 mm. For the welding process, the structure was welded using CO<sub>2</sub> gas-shielded welding. The equipment used was an inverter-type semi-automatic CO<sub>2</sub>/MAG arc welding machine with a gas flow rate of 15–20 L/min. The wire used was YC-YJ502 (Q) flux-cored wire with a wire diameter of 1.2 mm. Due to the thin plate thickness, no bevels were needed before welding. Welding joints were formed in one pass, with no need for multiple welds. The weld was first completed on one side of the T connection, then the torch was flipped over to the other side of the welding joint, followed by flipping the torch to weld the other side. The current, voltage, and welding speed for the two welds were shown in Table 1. For the welding sequence, the welding of the stringers with the plate was performed first, followed

by the welding of the longitudinal girders with the plate, and finally the welding of the transverse with the plate. The welding sequence was shown in Figure 3.

**Table 1.** Table of welding parameters.

No.	Current (A)	Voltage (V)	Velocity (mm/s)
1	142–155	22–25	6.2
2	138–147	20–22	6.1

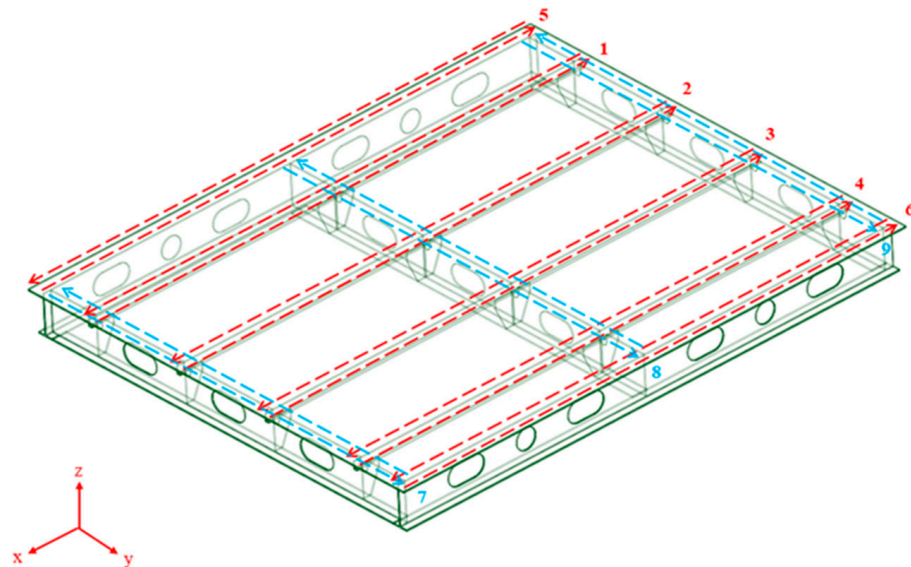


**Figure 3.** Diagram of the welding sequence.

### 3.2. Simulation of the Deformation and Stress of the Plated Grillage

Referring to actual welding data, the inherent deformation of the T connection was evaluated using the thermo-elastic-plastic finite element method. On this basis, the welding joint of the plated grillage was divided into parts, and the inherent deformation was applied to obtain the overall deformation and stress distribution.

#### 3.2.1. Calculation Method

Welding of the steel is a process of melting and re-solidification at the atomic level [33]. During the welding process, the presence of a large temperature gradient between the weld region and surrounding base material leads to an uneven distribution of residual plastic strain, which leads to the bending moment and out-of-plane welding deformation of the structure.

Currently, the two main finite element simulation methods for the welding process are the thermo-elastic-plastic finite element method and the inherent strain method. In this case, the thermo-elastic-plastic element method is first used to calculate the thermal loads applied to the mesh nodes from the heat source employing heat transfer and heat radiation. Subsequently, the mesh nodes on the structure are subjected to thermal loads generating displacements so that the stresses and deformations of the structure can be evaluated from the material's intrinsic relationship. This method can evaluate the stress and deformation of each mesh node throughout the welding process, but it is computationally expensive and takes a long time to compute for large structures [35].

To realize the rapid prediction of deformation and stress in large structures, Ueda et al. [36] conducted a series of experiments and theoretical derivations, and proposed an analysis method based on inherent strain, i.e., it is considered that the inherent strain is the fundamental cause of welding deformation and residual stress. Inherent strains  $\epsilon^{inherent}$



include thermal stress  $\epsilon^{thermal}$ , plastic strains  $\epsilon^{plastic}$ , creep strains  $\epsilon^{creep}$ , and transformation strains  $\epsilon^{transformation}$ , as shown in Equation (1).

$$\epsilon^{inherent} = \epsilon^{thermal} + \epsilon^{plastic} + \epsilon^{creep} + \epsilon^{transformation} \tag{1}$$

Since thermal strains disappear when the structure is cooled, and creep and transformation strains occur in small quantities compared to plastic strains, it is approximated in the calculations that the inherent strains are equal to the plastic strains. And due to the inhomogeneity of the plastic strain distribution, some simplifications are made in engineering applications. Due to the long length of the welding joint, the end effect is usually ignored, and the welding joint region is sectioned into separate areas to apply the inherent deformation to simulate the stresses and deformations generated in the whole structure [37]. During the finite element simulation, the strain can be converted to a thermal expansion coefficient according to Equation (2). The calculation of structural deformation and stress can be achieved by applying a unit temperature difference to the region of the welding joint where the inherent strain needs to be applied.

$$\epsilon_T = \alpha \cdot \Delta T \tag{2}$$

where,  $\epsilon_T$  is the inherent strain value,  $\alpha$  is the thermal expansion coefficient, and  $\Delta T$  is the unit temperature difference.

### 3.2.2. Calculation of the Inherent Deformation Data of Joints

The solid element model of the T joint was established, with a length and width of 400 mm, and a height of 250 mm. The height of the weld foot was 3 mm. The melt pool region was mesh-encrypted, and the number of elements and nodes were 24,950 and 34,218, respectively. The boundary conditions were set, as shown in Figure 4.

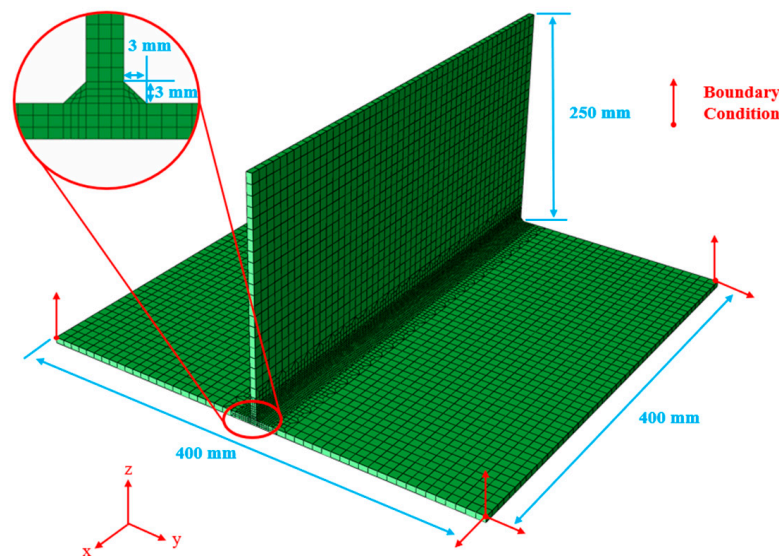


**Figure 4.** Diagram of solid element model of the T joint.

Based on the completion of the above setup and recorded actual welding parameters (as Table 1), the thermo-elastic-plastic finite element calculation of the T-joint was performed. In this section, the sequential coupling calculation method was adopted, i.e., the temperature field calculation was carried out first, and the stress and deformation of the joint were obtained by applying the temperature load to the mesh nodes after the calculation was completed. The material parameters of AH36 were shown in Figure 5.

For the computed temperature, the maximum temperature of the joint was 2075 °C. As was shown in Figure 6, the region where the temperature was higher than the melting point of the steel was essentially the same as the geometry of the melt pool. Then, the

temperature load was applied to the structure and the computed deformation as well as plastic strain distribution was shown in Figures 7 and 8. In Figures 7 and 8, NT11 is the nodal temperature ( $^{\circ}\text{C}$ ), U is the deformation (mm), and PE11, PE22, and PE33 are the plastic strains in the x, y, and z directions, respectively.

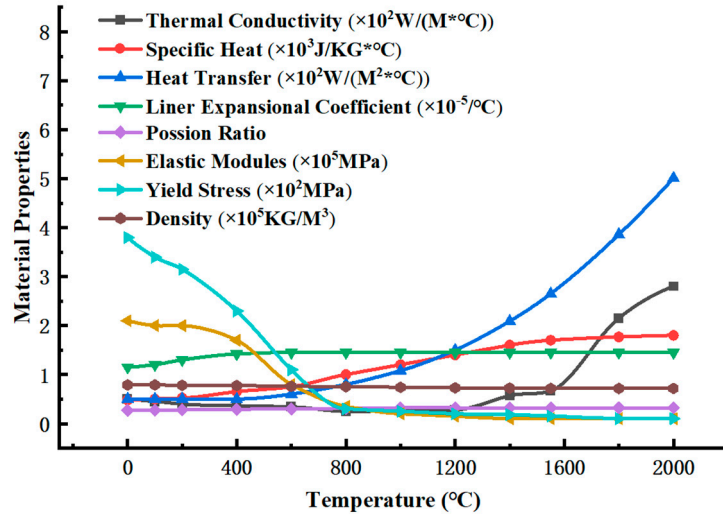


Figure 5. Diagram of the material parameters of AH36.

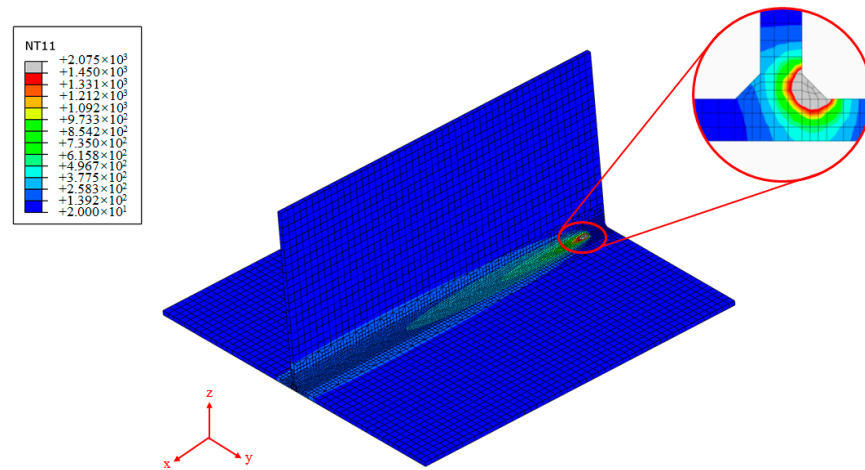


Figure 6. Diagram of the computed temperature distribution.

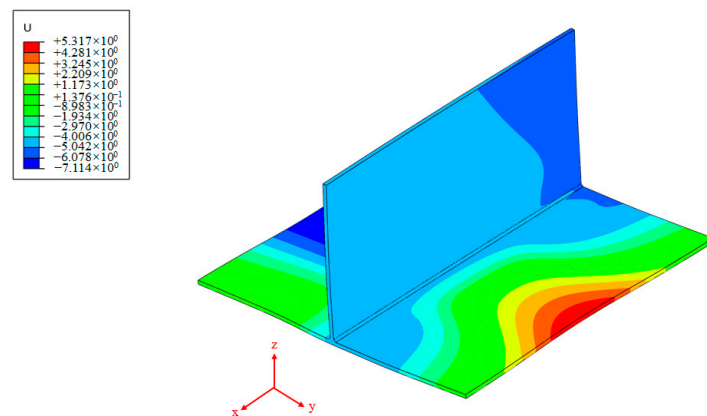
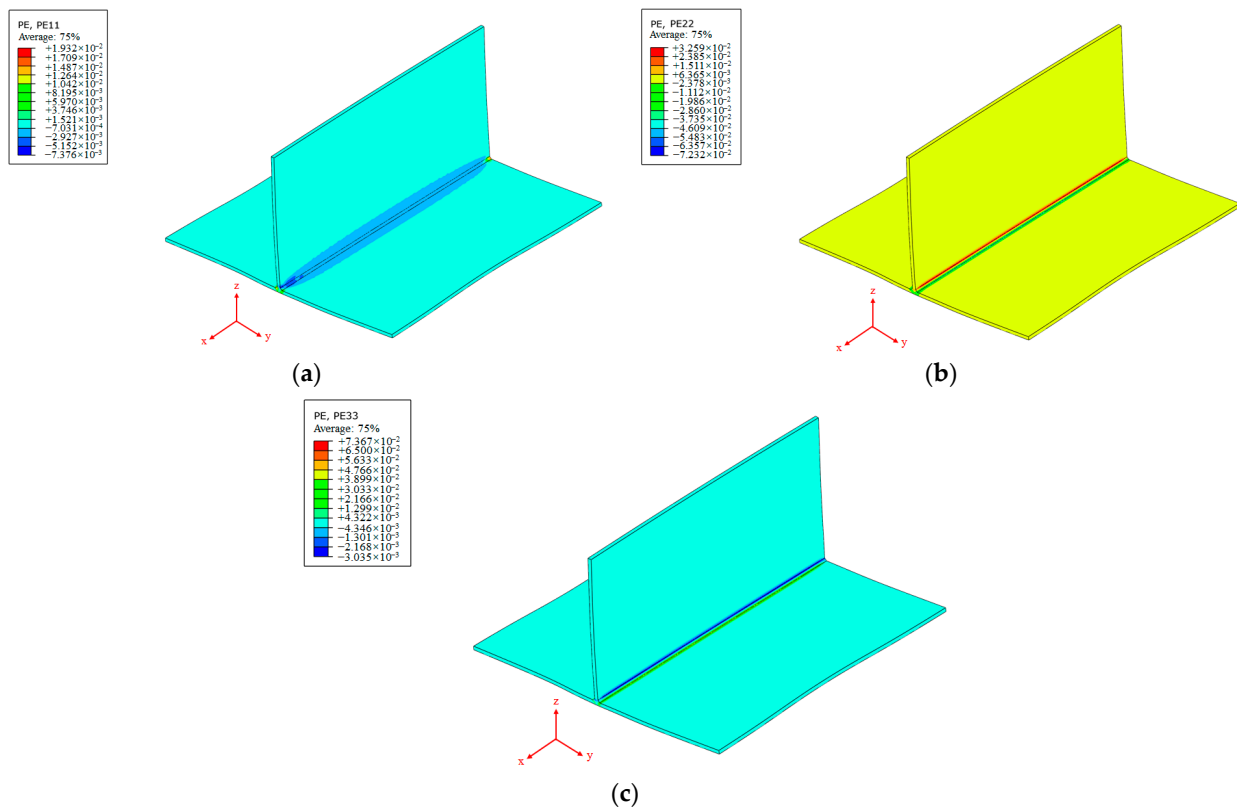


Figure 7. Diagram of the computed deformation.



**Figure 8.** Diagram of the computed plastic strain distribution. (a) Longitudinal plastic strain, (b) transverse plastic strain, and (c) vertical plastic strain.

As was shown in Figure 8, the plastic strain values around the welding joint were higher. In the following section, the plastic strain in this region was extracted and converted to thermal expansion coefficients referring to Equation (2) to be assigned to the welding joint regions of the plated grillage for the calculation of its deformation and stress distribution.

### 3.2.3. Welding Deformation and Stress Computation of Plated Grillage

On the basis of the computation to obtain the joint inherent strain data in Section 3.2.2, the application of the inherent strain on the plated grillage was carried out. After analyzing the results of the T joint computation, it was found that the plastic strain distribution in the molten pool region was distinctly inhomogeneous in the Z-direction. Particularly for plastic strains in the Y- and Z-directions, there was a distinct difference between tensile and compressive strains (as shown in Figure 9).

Due to the inhomogeneous distribution characteristics of the plastic strain at the weld obtained from the joint calculations along the Z-direction, the plated grillage was subjected to the operation of partitioning and applying different inherent deformations to obtain a higher accuracy of calculation. The partitioning approach for the welding joints between the plate and longitudinal girder, stringer, and transverse was shown in Figure 10. The thermal expansion coefficients of the material corresponding to the unit temperature difference obtained referring to Equation (2) were shown in Table 2.

**Table 2.** Table of the thermal expansion coefficients.

Direction	Thermal Expansion Coefficients	
	Region-A	Region-B
Longitudinal	−0.00233	−0.00248
Transverse	−0.010	0.016
Vertical	0.0126	−0.0254

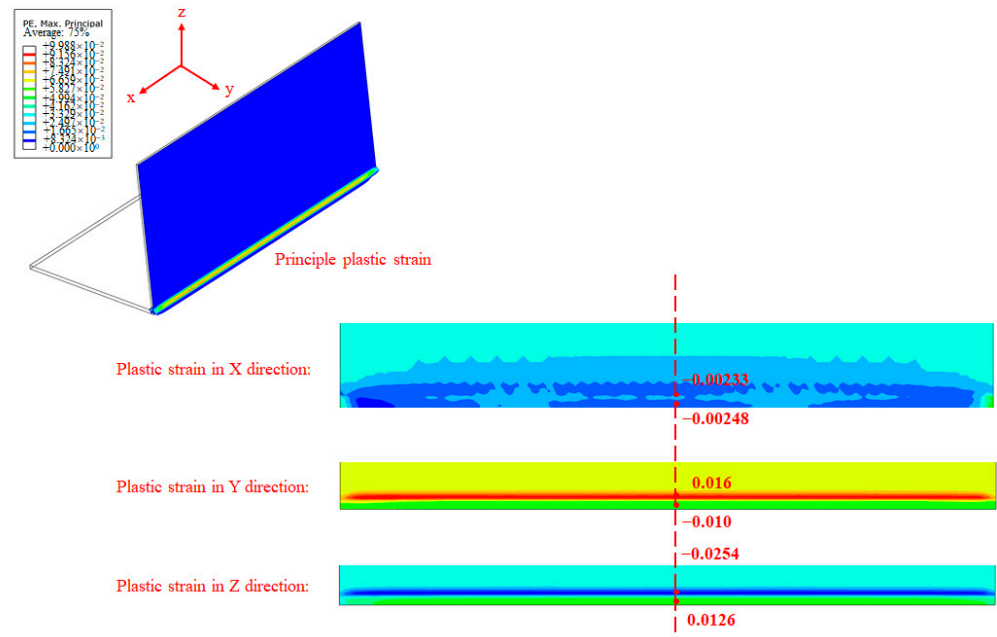


Figure 9. Diagram of the plastic strain distribution in the molten pool.

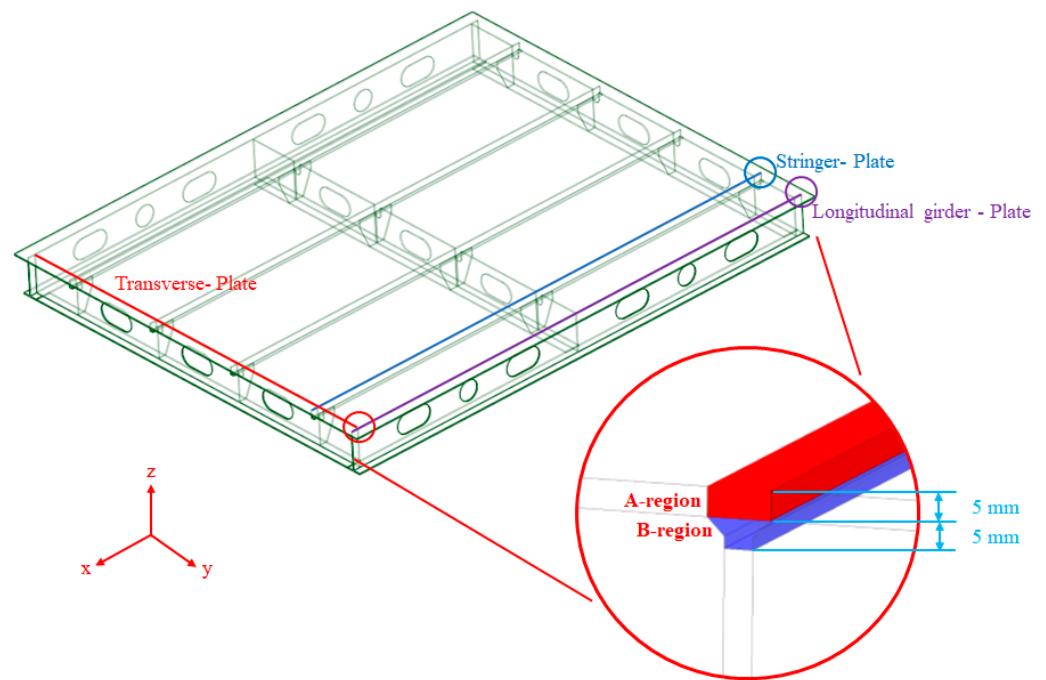


Figure 10. Diagram of the partitioning approach for the welding joints.

After determining the partitioning of the welding joint and the inherent deformations to be imposed, a solid element model was established. The deformation and stress distribution of the plated grillage were simulated using the ABAQUS (2022) software on an 8-core (4.5 GHz) 16-threaded PC with 64 GB of RAM. The computational time for a single model was about 55 min.

The model is meshed using hexahedral elements, with the element type C3D8R, and the number of elements and nodes were 665,548 and 779,472, respectively. Encryption of the mesh was conducted in the heat-affected region around the welding joints. The boundary conditions were set not to unduly restrict the degrees of freedom of the structure and to ensure that the constraints of the specimen were close to the actual assembly welding

process [34]. The detailed boundary condition settings were shown in Figure 11. The stress distribution and deformation of the plated grillage were shown in Figures 12 and 13.

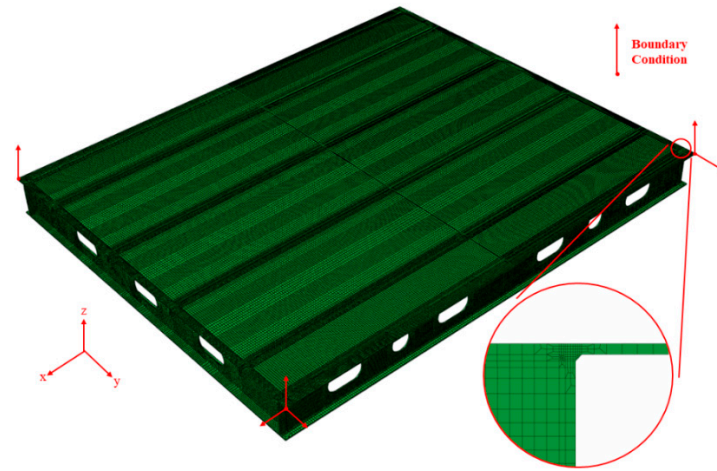


Figure 11. Diagram of solid element model of the plated grillage.

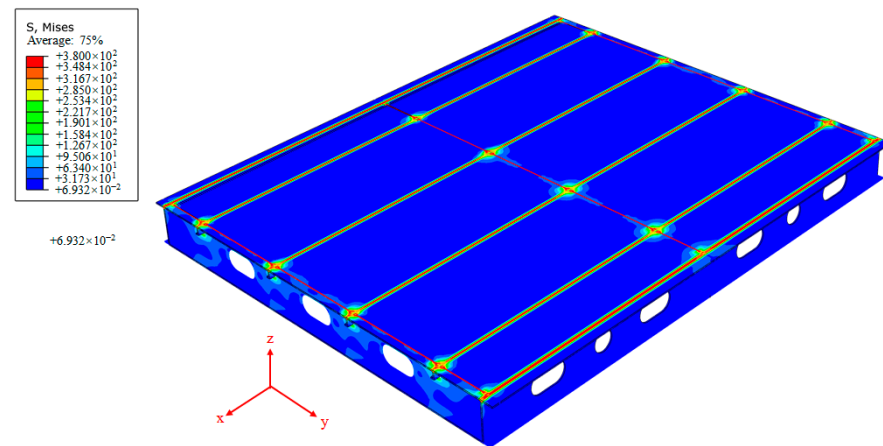


Figure 12. Contour diagram of stress distribution in the plated grillage.

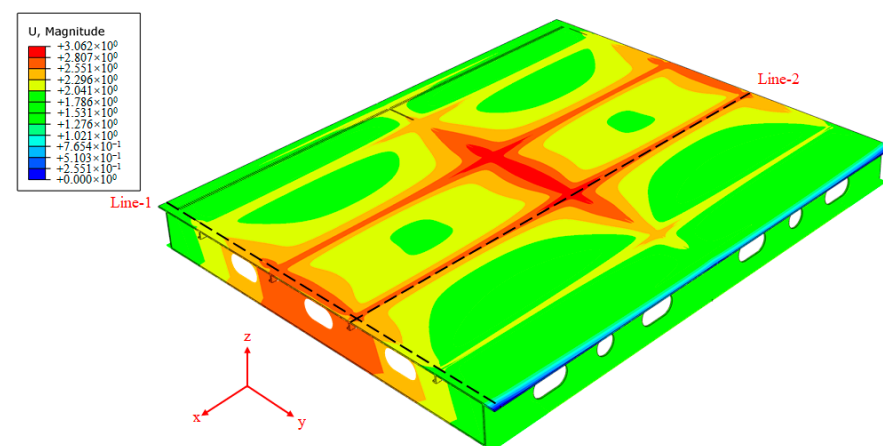


Figure 13. Contour diagram of deformation distribution in the plated grillage.

As shown in Figures 12 and 13, there are relatively high stresses in the welding joint region that reached the yield strength of the material, causing plastic deformation. A certain number of high-stress areas were also presented in the transverse due to the shrinkage of the welding joint of the longitudinal stringers. For the deformation condition, the maximum deformation on the plated grillage is about 3.1 mm. To verify the agreement between



the simulated and measured deformation of the plated grillage, two monitoring lines (as Figure 13) were set up above the plate region connecting with the longitudinal stringer and transverse, and the simulated and measured vertical deformation values were compared. Deformation values were measured using an XTDIC 3D optical acquisition system with a measurement accuracy of  $\pm 0.1$  mm. Data collection was performed at 100 mm intervals in the length and width directions of the specimen, with the number of collection points being 20 and 16, respectively (as shown in Figure 14). Comparison results were shown in Figure 15.



Figure 14. Diagram of the actual plated grillage specimen.

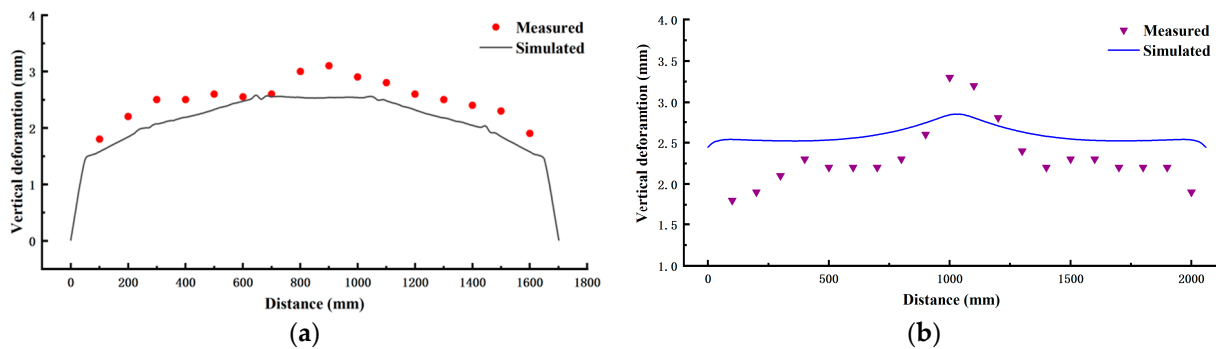


Figure 15. Diagram of the deformation comparison results of monitoring lines. (a) Line 1 and (b) line 2.

As shown in Figure 15a,b, the deformation values of the monitoring lines fluctuated significantly at the welding joint. The monitoring line 1 direction presented a large amount of deformation due to the denser welding joint arrangement, and the maximum value of the simulated vertical deformation results reached 2.58 mm. The measured values corresponded well to the simulated values. The fluctuation of the deformation in the monitoring line 2 direction was small, with only a small peak around the welding joint region of the middle transverse. When the specimen was manufactured, there was a splice weld in the middle of the deck due to the limitations of the available plate sizes. Although the deck splicing was corrected after completion, it still resulted in a large error in the measurements at the center. Measured values away from the splice seam region were in good agreement with the simulated values.

#### 4. Investigation of the Failure Buckling Behavior of Combined Opening Plated Grillage Considering the Initial Welding State

##### 4.1. Numerical and Experimental Basis

The nonlinear finite element method was applied to calculate the failure behavior of the plated grillage. The welding deformation and residual stresses calculated in Section 3 were also applied as initial states to investigate their effect. On this basis, static load experiments were designed and performed, and the experimental results were compared with the simulated values to verify their reliability.

#### 4.1.1. Simulation Settings

The nonlinear finite element calculation of the plated grillage was also conducted using ABAQUS (2022) software. The calculated welding deformations and stresses were applied as the initial load to the plated grillage model for further failure analysis. The meshes were divided in the same forms as used in the inherent strain calculation above, and the element type is C3D8R. The material parameters of the specimen were kept the same as mentioned in the welding simulation above. The Young's modulus of the material was 206 GPa and the yield strength was 380 MPa at 20 °C. The tangential modulus of the material was mostly taken as 5–15%, and there it was taken as 10% in combination with the results of the tensile experiments (as Figure 16). The specimen size for the tensile experiment was determined according to the Chinese national standard (GB-T 228.1-2021) [38].

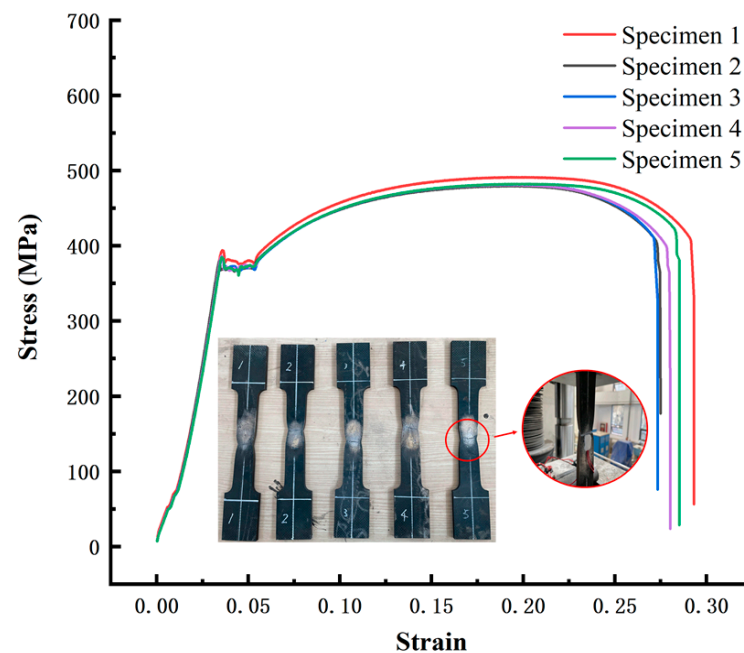


**Figure 16.** Diagram of the tensile experiment results.

In the previous experiments on the combined opening girders, it was found that the structure would fail in a complex manner such as instability and local buckling under the central vertical load applied from the plate [39]. Most of the existing plated grillage experiments focused on the failure behavior under longitudinal and transverse compressive loads, ignoring the effect of vertical bending loads from the plate [28,29]. Therefore, two loading conditions were designed. One was to load an area with a 200 mm width in the middle of the longitudinal direction. The other is to load an area with a 200 mm width in the middle of the transverse and longitudinal directions in combination. For the setting of boundary conditions, the main consideration is the support of the surrounding pillars for the plated grillage, so the position of the plated grillage and pillar connections were equivalently replaced by fixed constraints, and the failure behavior of the plated grillage under bending loads was mainly investigated. The loading method and boundary condition settings were shown in Figure 17.

In Figure 17,  $R_x$ ,  $R_y$ , and  $R_z$  are the rotational degrees of freedom in the  $x$ -,  $y$ -, and  $z$ -axis; and  $U_x$ ,  $U_y$ , and  $U_z$  are the translational degrees of freedom.

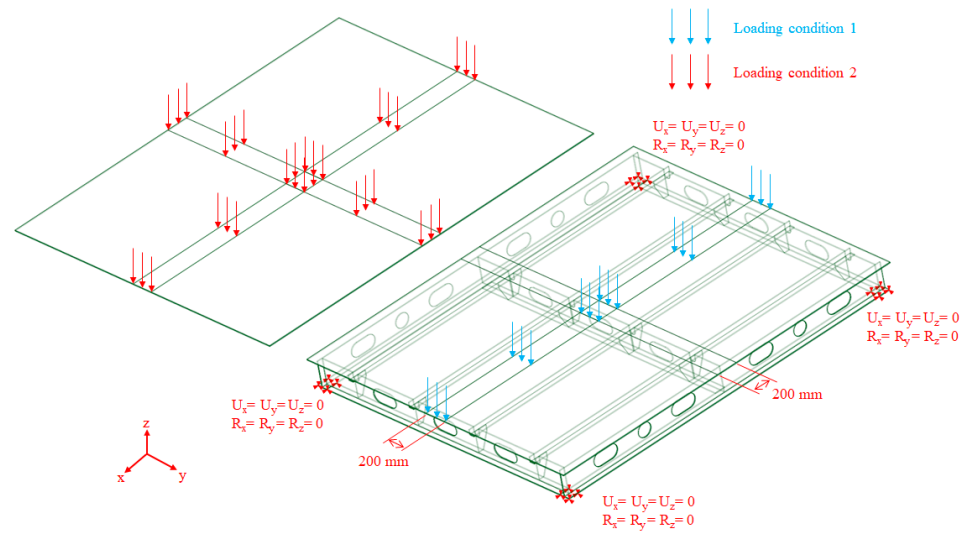


Figure 17. Diagram of the loading conditions and boundary condition settings.

#### 4.1.2. Experiment Design

The vertical loading of the specimen was applied using a 4000 kN thrust servo actuator. To realize the two load conditions described in Section 4.1.1, the corresponding design of the distribution girders was performed. The experiment scenario was shown in Figure 18.

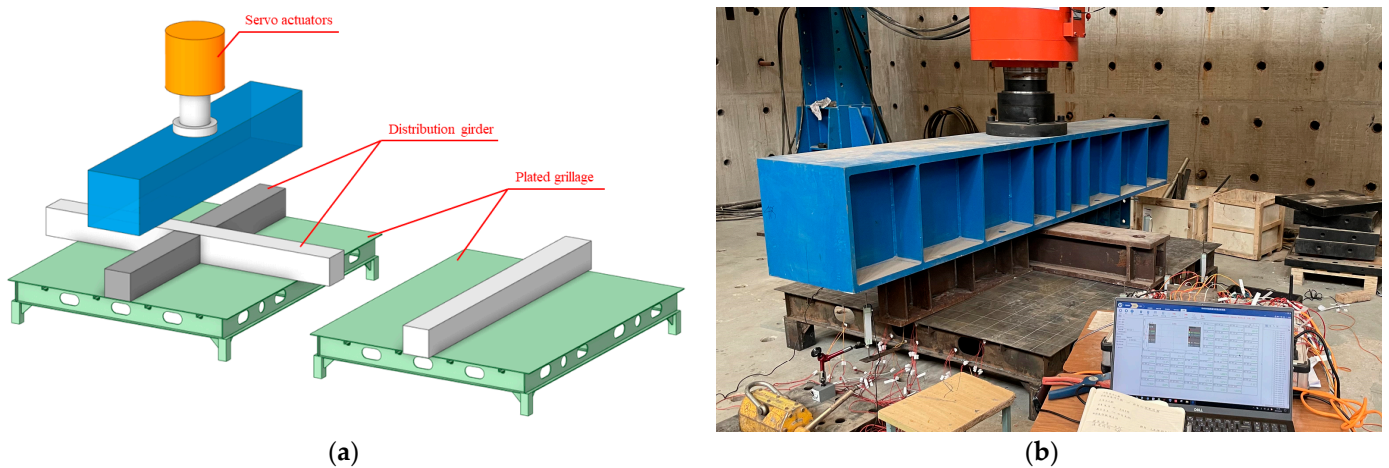


Figure 18. Diagram of the experimental scenario. (a) Schematic model and (b) physical scenes.

To collect the strain and stress in the plated grillage, displacement gauges were arranged at several typical points and strain gauges (rosettes) were attached to the steel surface. The type of displacement gauge was YWD and the measurement accuracy was  $\pm 0.01$  mm. The types of strain gauges and rosettes were BFH120-2CA-D150 and BFH120-2AA-R-P300, respectively, with sensitivity coefficients of  $2.0 \pm 1\%$ . The arrangement of displacement gauges and strain gauges (rosettes) was shown in Figure 19.

During the conducting of the experiment, the force-controlled loading method was first applied at the linear deformation stage of the plated grillage, with 20 kN per step. When approaching the plastic deformation stage, the displacement-controlled loading method was applied, with 1 mm per step. Then the loading was maintained until the value of the vertical pressure recorded by the pressure transducer dropped to 50% of the peak load value. At this point, the loading was stopped, and the experiment was completed.

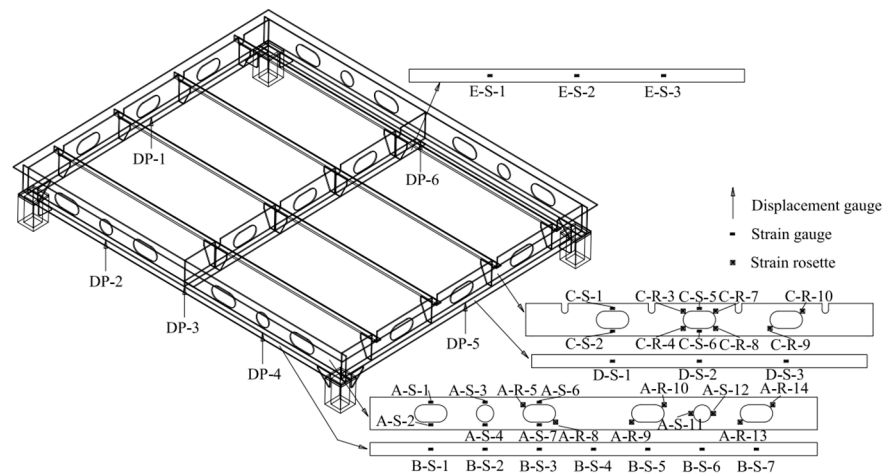


Figure 19. Diagram of arrangement of measurement gauges.

#### 4.2. Experiment and Simulation Results

##### 4.2.1. Load-Displacement Relationships

Due to the differences in the loading method, the two specimens exhibited different deformation and failure behaviors. In this section, the values of three displacement gauges (DP-1, DP-3, and DP-5) were selected for comparison. Meanwhile, the vertical displacement values of the plate center point obtained from simulation and measurement (considering the initial welding state) were compared. The load-displacement curves were shown in Figure 20.

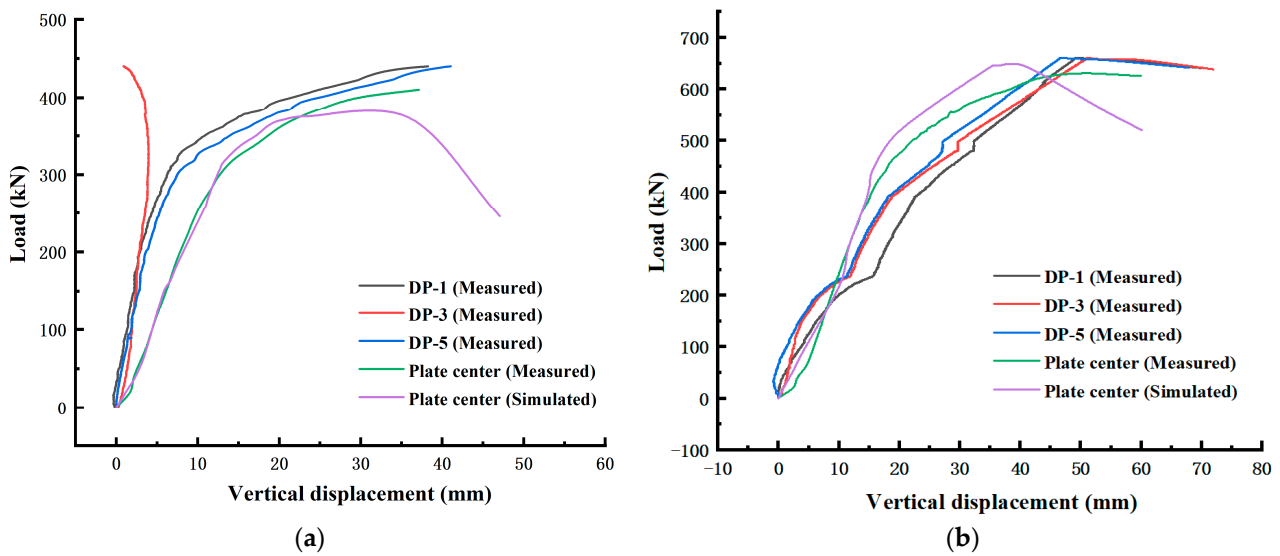


Figure 20. Diagram of the load-displacement curve. (a) Condition 1 and (b) condition 2.

For the first loading condition, the maximum load that the structure could bear was about 430 kN. As shown in Figure 20a, as the loading region was an area of 200 mm width in the middle of the longitudinal direction, and the middle of the front and back transverse exhibited similar displacement regulations under vertical loads. The location of the middle point of the plate also showed a similar displacement regulation to the DP-1 and DP-3 regions under the action of the distribution girder. For the values measured from DP-1, since the region was far away from the loading region, less vertical displacement occurred. As for the whole loading process, when the load is in the range of 0–300 kN, the structure was in the stage of elastic deformation. With the increase in the external load, the vertical displacements of all four measurement points increased linearly. When the external load

exceeded 300 kN, the structure gradually entered the plastic deformation stage. The slopes of the load-displacement curves at points DP-1, DP-5, and the plate center became smaller, and the structure experienced a distinct vertical displacement. The position of measurement point DP-3 was rotated around the X-axis due to the middle deformation of the structure; the position of the displacement gauge was shifted, so the measured displacement values appeared to decrease with the increase in the external load. Next, as the external load further increased to reach the critical load of the structure, there was a sudden loss of the load-bearing capacity of the structure. The loading device stopped loading for protection, so the measured curve in the figure terminated at the highest load point and did not record the post-buckling characteristics of the structure. The simulated load-displacement curve of the plate middle point fitted well with the measured curves and reflected a certain degree of post-buckling characteristics.

For the second loading condition, the maximum load the structure could bear was about 660 kN, with an improvement of 53.49% compared to the loading condition 1. As shown in Figure 20b, as the loading region was a combined area of 200 mm in the middle of both the longitudinal and transverse directions, the middle of the left and right longitudinal girders as well as front and back transverse exhibited similar displacement regulations for the load applied by the distribution girder. For the loading process, when the load is in the range of 0–600 kN, the structure was in the stage of elastic deformation. As the external load increased, there was a slow linear increase in the vertical displacement of the structure. When the external load reached 600 kN, the structure entered the plastic deformation stage, the rise of the load slowed down, and the structure suffered distinct vertical displacement. However, differing from the failure characteristics of the sudden loss of the load-bearing capacity of the structure in loading condition 1, in loading condition 2, when the structure entered into the plastic deformation stage, the external load remained stable with the distinct increase in displacement. The external load on the structure gradually decreased only when the vertical displacement exceeded 50 mm. The structure exhibited a considerable load-bearing capacity in the post-buckling phase.

#### 4.2.2. Deformation

Combining the results of experiments and simulations, the failure behaviors of the plated grillage were investigated. The deformation of the structure after failure was shown in Figure 21.

As shown in Figure 21, the simulated failure behavior of the plate, longitudinal girders, and transverses were basically consistent with the results obtained from the experiment. For loading condition 1, owing to the vertical load applied to the area of a 200 mm width in the middle of the longitudinal direction, the plated grillage exhibited a bending deformation in the middle region. The transverses, which bore most of the loads as the main transverse component, suffered distinct deformation. In contrast, the section modulus at the opening region in the transverses was greatly reduced due to the presence of lumbar round openings. The bending load experienced a transmission discontinuity at the lumbar round opening regions, and the transmission path was shifted. Stress concentrations appeared at the corners of openings, resulting in a localized plastic hinge failure phenomenon (as Figure 21a). In addition, under this loading method, the longitudinal girders were arranged parallel to the direction of the loading region in the center, and no distinct deformation occurred. Only the rotation of the whole longitudinal girders along the X-axis direction occurred with the increase in the external load.

For loading condition 2, owing to the loading region being an area of a 200 mm width in the middle of the transverse and longitudinal directions, both longitudinal girders and transverses participated in load-bearing. Subjected to external loads, the middle regions of the left and right longitudinal girders as well as the front and back transverses exhibited distinct vertical deformations. Due to the action of distributing girders, the vertical deformation in the middle region of these major longitudinal and transverse components was consistent. Similarly, the longitudinal girders and transverses showed a localized plastic



hinge failure around the lumbar round opening regions in loading condition 1. As for the longer length of the longitudinal girders, the plastic hinge deformation phenomena were more pronounced at the lumbar round openings closer to the middle loading region than at the distal end.

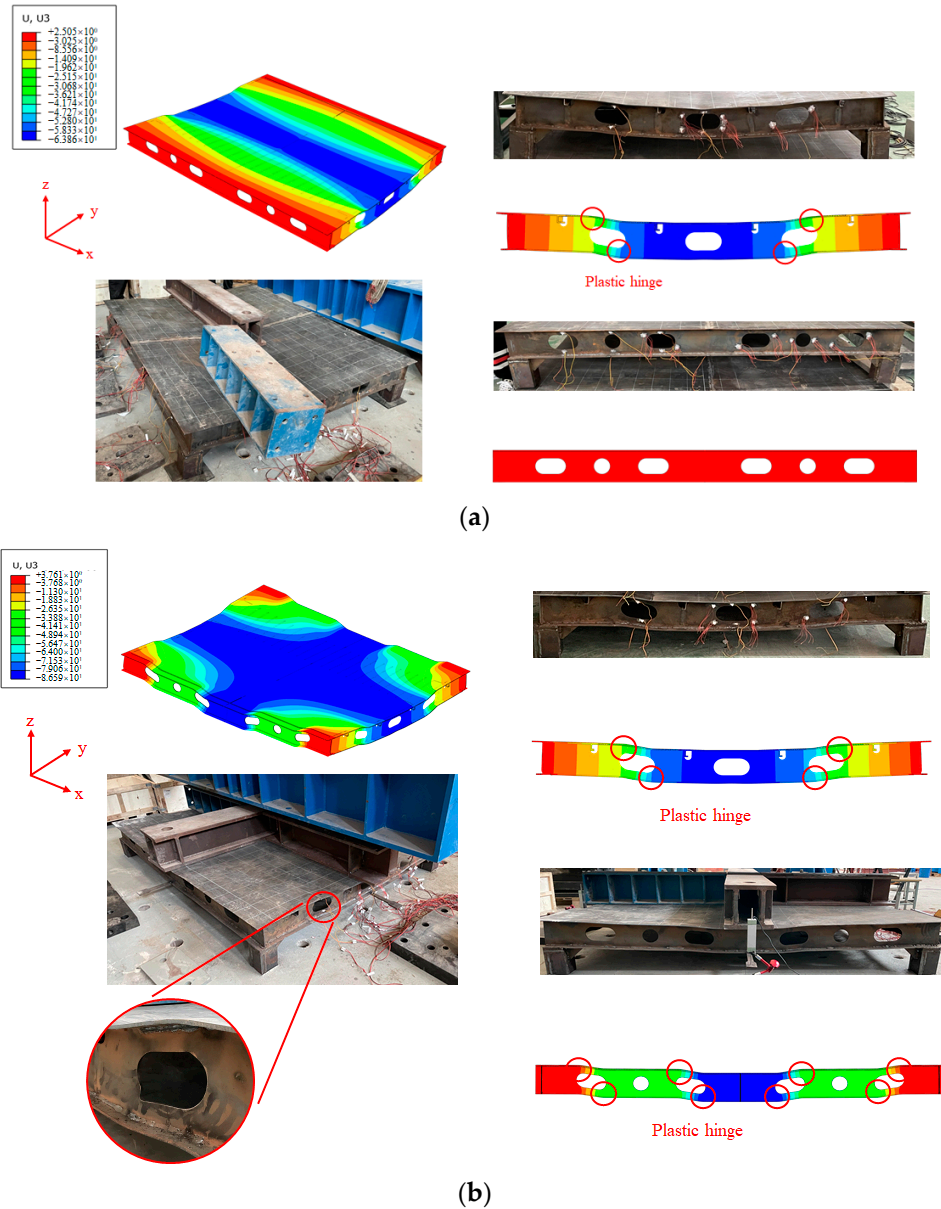
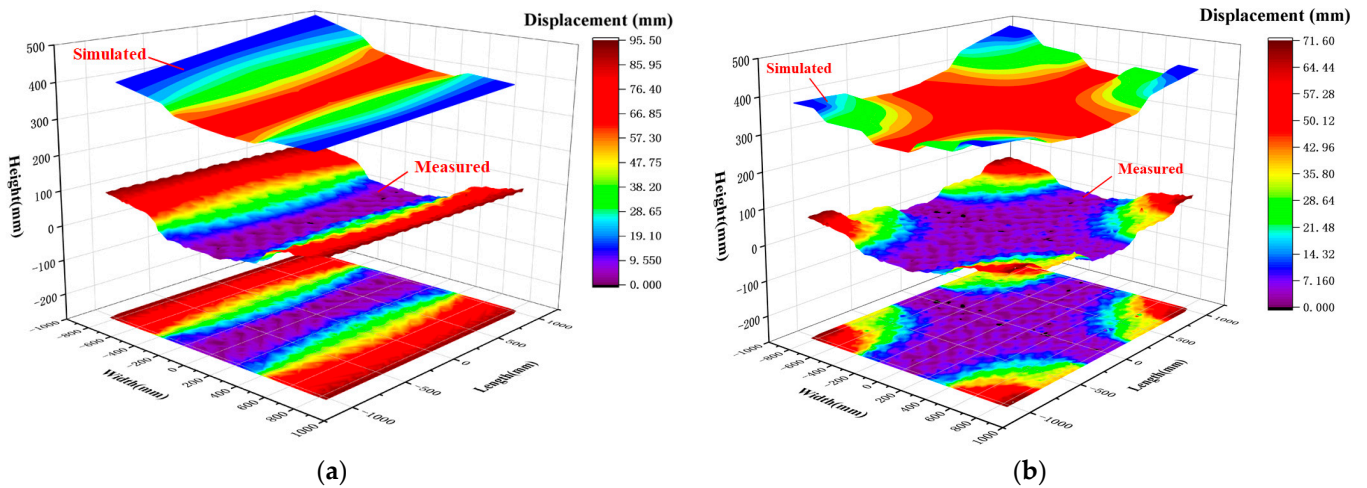


Figure 21. Diagram of the failure behaviors. (a) Condition 1 and (b) condition 2.

For two loading conditions, the central region of the transverses presented a significant vertical deformation. In contrast, in the static load experiments of the girders in the literature 39, the girder structures presented a phenomenon of instability due to the occurrence of lateral slip in the middle region. It could be seen that the inclusion of the ribs in the plated grillages could limit the local instability phenomenon of the structure and improve the load-bearing characteristics.

In addition, to investigate the deformation regulations of the plate of the plated grillages and verify the agreement between the simulation and experiment results, the coordinates of the measuring points on the deformed plate surface were measured by the XTDIC 3D optical acquisition system. The curved surfaces were formed based on the fitting of coordinate values and compared with the results of simulations. The comparisons were shown in Figure 22.



**Figure 22.** Diagram of the simulated and measured comparison results of plate deformation. (a) Condition 1 and (b) condition 2.

As shown in Figure 22, the curved surface shapes obtained from the fitting of the measured data were in good agreement with the results of the simulation. For loading condition 1, the plate exhibited a buckling band similar to a hyperbolic symmetrical arrangement on both sides of the longitudinal center of the plate (as Figure 22a). The entire plate showed a vertical deformation approximating the shape of a cylinder in the region between the two lumbar round openings along the X-axis. As for loading condition 2, there are significant differences in the deformation patterns of the plate. The vertical displacement values of the central region in both the X and Y axes were approximately equivalent. The plate exhibited a gradual increase in vertical displacement from the corners to the middle region in both the X and Y directions. Both directions showed a localized bending of the plate above the lumbar round openings, resulting in a significant change in vertical displacement on both sides of the bend. From the corners toward the center of the plate, buckling bands similar to the inverse function distribution appeared (as Figure 22b).

#### 4.2.3. Stress and Strain

Due to the differences in the loading conditions, there were significant differences in stress distribution in the plate frame at failure. For loading condition 1, the stress level on the longitudinal girders was low and there was no significant stress concentration around the opening regions. The transverses, due to bearing most of the external loads, showed a high-stress region in the middle of the stiffener flange and a significant stress concentration around the opening. For loading condition 2, both the longitudinal girders and transverses were involved in bearing the external loads, so the stress levels were higher in the middle of the stiffener flange. Meanwhile, there were stress concentrations at the corners of the lumbar round openings. The stress distribution was shown in Figure 23.

Referring to the stress distribution, it could be seen that due to the difference in the loading conditions, there was a significant difference in the stress level in the middle of the stiffener flange of the longitudinal girders and transverses. The strain values measured experimentally at this location are discussed next. The values on the surface of specimens during the experiment could be measured by strain gauges (rosettes). The selected measuring points were numbered B-S-4 and D-S-2. The strain values of the measuring points were shown in Figure 24.

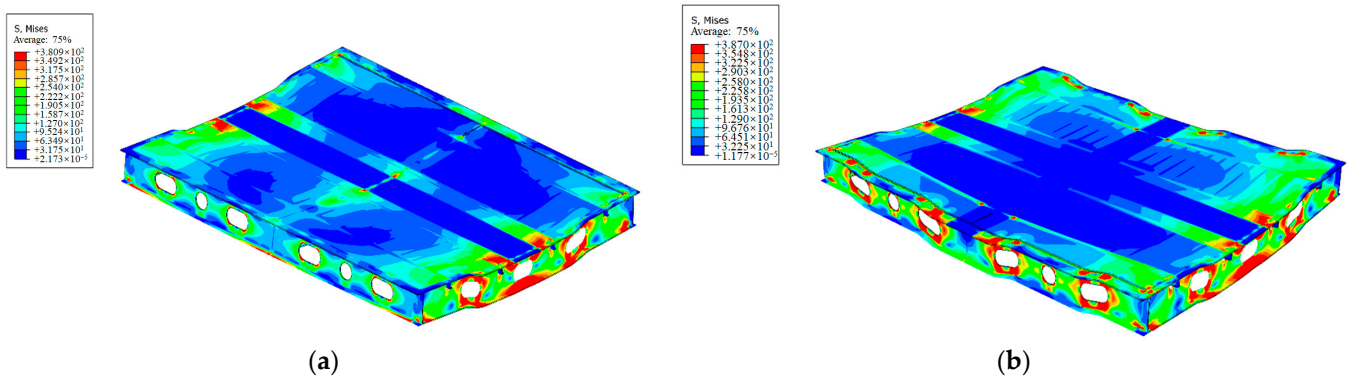


Figure 23. Contour diagram of stress distribution in the plated grillage. (a) Condition 1 and (b) condition 2.

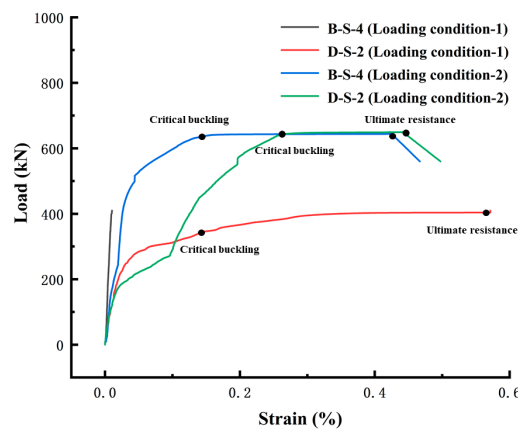
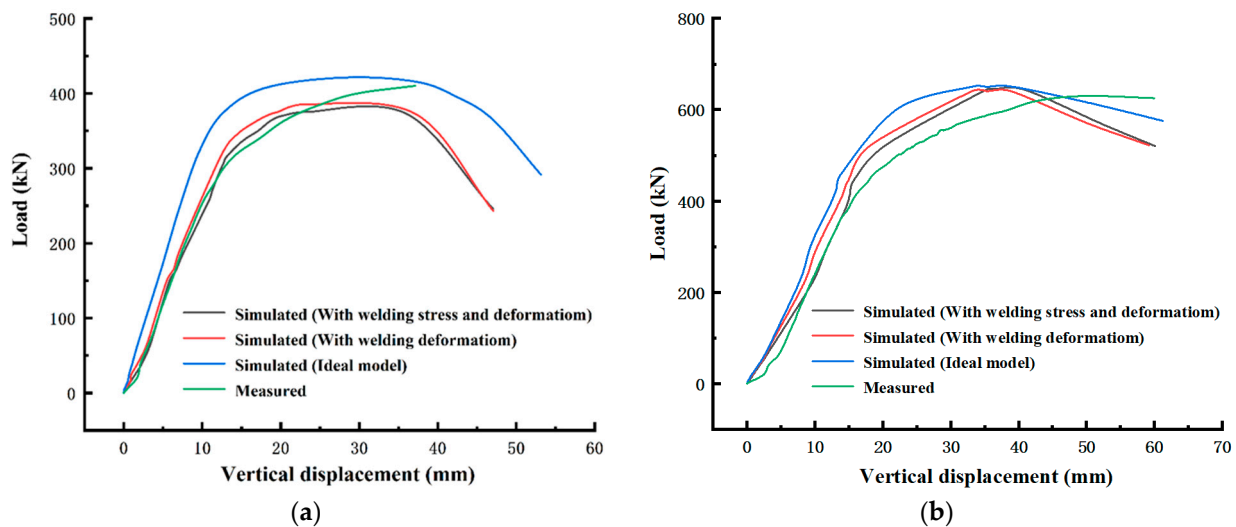


Figure 24. Diagram of the strain values of the measuring points.

As shown in Figure 24, for loading condition 1, since the main load in this loading method was borne by the transverses, the strain measured from the location of the measuring point on the longitudinal girder was small, less than 0.1%. The strain measured from the location of the measuring point on the transverse was large, especially when the external load reached 370 kN, the strain value increased rapidly, and the structure lost its load-bearing capacity. For loading condition 2, since both the longitudinal girders as well as the transverses were involved in load-bearing, the strain values measured at the locations of the two measurement points were large. In the pre-loading stage, the transverses were subjected to a large load, producing a more pronounced strain. When the external load came to 450 kN, the longitudinal girders also participated in the load-bearing, and the strain growth rate increased significantly. In this case, the increased rate of strain at the measuring point on the longitudinal girder was larger than that on the transverse. When the external load reached 610 kN, the strain values at the two measuring points gradually reached the same and increased rapidly; at this time, the structure gradually lost its bearing capacity.

#### 4.3. Influence of the Initial Welding State on Structural Load-Bearing Behaviors

The degree of congruence between the numerical results was verified above. With the use of the inherent strain method, the distribution of stresses and deformations of specimens generated during the welding process was also simulated. In this section, the load-bearing behavior of the ideal model, the model considering initial deformation, and the model considering initial deformation and stresses were compared for two loading conditions using numerical means. The load-displacement relationship curves of the plate center point for these conditions were shown in Figure 25.



**Figure 25.** Diagram of the load-displacement curve considering the initial welding state.

As shown in the Figure 25, considering the initial welding state of the specimens, the ultimate load-bearing capacity decreased slightly compared to the ideal model and had a better fit to the experimental load-displacement curves. For loading condition 1 in the Figure 25a, the curve considering welding residual stresses and deformations almost coincided with that only considering deformation. For the welding parameters used in this structure, the welding residual stresses had almost no effect on the deformation structure in the elastic phase. As the external load continued to increase, the residual stresses made the structure more susceptible for plastic deformation while leading to a 2.5% reduction in the ultimate load-bearing capacity. Next, comparing the curves considering only the welding deformation with those of the ideal model, it was evident that the welding deformation has a significant effect on the deformation behavior of the structure. In the elastic phase, the welding deformation enabled the structure to generate a larger vertical displacement under the same external load and entered the plastic phase earlier. The ultimate load-bearing capacity showed a decrease of 8.6%.

For loading condition 2 in the Figure 25b, compared to welding deformation, the effect of welding residual stresses on the deformation behavior of the structure remained insignificant. The load-displacement curves for the two cases nearly overlapped, with only a small difference in the position at which the structure entered the plastic phase. Next, compared with the curve of the ideal model, the presence of welding deformation accelerated the vertical displacement of the structure in the elastic phase, causing the structure to yield earlier. However, the influence degree was less than that in loading condition 1. When the structure failed, the ultimate load-bearing capacity of the structure was essentially the same in all three cases. It may be seen that under this loading mode, the welding residual stresses and deformations caused by the welding parameters used in this specimen had basically no effect on the ultimate load-bearing capacity of the structure.

## 5. Conclusions

A simulation method that partitions the welding joint region to apply different inherent strains was used to calculate the initial welding deformation and stress based on actual welding parameters. Then the results obtained from the calculations were used as an initial state for nonlinear finite element calculations, and the deformation behaviors of the structure were simulated and compared with the results of the static load experiments.

The main findings are as follows:

- (1) The method of partitioning the welding joint region to apply different inherent strains could enable a more accurate prediction of welding deformation and stress distribution in the plated grillages. Referring to its simulation results, the welding deformation

of the plated grillage was mainly angular deformation caused by welding shrinkage at the connection of the longitudinal stringers, longitudinal girders, and transverses with the plate.

- (2) For the plated grillage, when the loads were carried by a combination of longitudinal and transverse components, the structure had a high ultimate load-bearing capacity. When the structure reached the ultimate load-bearing limit, the structure still had a considerable load-bearing capacity in the post-buckling phase. For loading conditions in which the load was applied to the components in a single direction, the ultimate load-bearing capacity of the structure was greatly reduced. And there was a phenomenon that the overall structure lost its load-bearing capacity due to localized structural failures.
- (3) The degree of influence of welding deformation and stress on the structural load-bearing behavior was related to the method of applying the external loads. When the vertical load was carried by a combination of longitudinal and transverse components, the overall load-bearing state of the structure was more stable, and the influence of welding factors on the ultimate load-bearing capacity of the structure was small. When the transverse members were mainly involved in load-bearing, the structure suffered from localized deflections of the whole longitudinal components. Welding factors would exacerbate this phenomenon, resulting in a significant reduction in the overall ultimate load-bearing capacity.
- (4) Higher stiffener web heights could exacerbate the instability of the structure under vertical loading, and lateral movement of the central parts of the structure occurred, leading to localized instability. Meanwhile, the plastic hinge failure behavior at the corners of the lumbar round openings was associated with a loss of the structural load-bearing capacity. The addition of ribs could improve the local failure behavior of the structure and increase the load-carrying capacity.

**Author Contributions:** Conceptualization, C.C., H.Z. and Z.L. (Ziqiu Li); methodology, C.C. and Z.L. (Zhengda Lv); software, C.C. and Z.L. (Zhengda Lv); investigation, C.C. and Z.L. (Ziqiu Li); resources, H.Z.; writing—original draft preparation, C.C.; writing—review and editing, C.C. and H.Z.; visualization, H.Z.; supervision, H.Z.; project administration, H.Z.; funding acquisition, H.Z. All authors have read and agreed to the published version of the manuscript.

**Funding:** This research was funded by the National Natural Science Foundation of China (52371323) and the Postgraduate Research & Practice Innovation Program of Jiangsu Province (KYCX22\_3838).

**Institutional Review Board Statement:** Not applicable.

**Informed Consent Statement:** Not applicable.

**Data Availability Statement:** The data used to support the findings of this study are available from the corresponding author upon request.

**Acknowledgments:** The authors would like to acknowledge the financial support provided by the National Natural Science Foundation of China (52371323) and the Postgraduate Research and Practice Innovation Program of Jiangsu Province (KYCX22-3838), and also acknowledge Shanghai Waigaoqiao Shipbuilding Co., Ltd. and China Shipbuilding Cruise Technology Development Co. Ltd. for their support in conducting relevant experiments.

**Conflicts of Interest:** The authors declare no conflict of interest.

## References

1. Shen, W.; Zhao, Y.; Li, L.; Qiu, Y.; Liu, E. Assessment of residual ultimate strength on plate girders with web opening under compression-bending loadings. *Ocean Eng.* **2019**, *187*, 106147. [[CrossRef](#)]
2. Zhao, Y.; Yan, R.; Wang, H. Experimental and numerical investigations on plate girders with perforated web under axial compression and bending moment. *Thin-Walled Struct.* **2015**, *97*, 199–206.
3. Liu, X.; Guo, Z.; Bai, D.; Yuan, C. Study on the mechanical properties and defect detection of low alloy steel weldments for large cruise ships. *Ocean Eng.* **2022**, *258*, 111815. [[CrossRef](#)]
4. Brown, C.J.; Yettram, A.L. The elastic stability of square perforated plates under combinations of bending, shear and direct load. *Thin-Walled Struct.* **1986**, *4*, 239–246. [[CrossRef](#)]



5. Shakerley, T.; Brown, C. Elastic buckling of plates with eccentrically positioned rectangular perforations. *Int. J. Mech. Sci.* **1996**, *38*, 825–838. [[CrossRef](#)]
6. Brown, C. Elastic buckling of perforated plates subjected to concentrated loads. *Comput. Struct.* **1990**, *36*, 1103–1109. [[CrossRef](#)]
7. El-Sawy, K.M.; Nazmy, A.S.; Martini, M.I. Elasto-plastic buckling of perforated plates under uniaxial compression. *Thin-Walled Struct.* **2004**, *42*, 1083–1101. [[CrossRef](#)]
8. Shanmugam, N.E.; Lian, V.T.; Thevendran, V. Finite element modelling of plate girders with web openings. *Thin-Walled Struct.* **2002**, *40*, 443–464. [[CrossRef](#)]
9. Shanmugam, N.E.; Thevendran, V.; Tan, Y.H. Design formula for axially compressed perforated plates. *Thin-Walled Struct.* **1999**, *4*, 1–20. [[CrossRef](#)]
10. Paik, J.K. Ultimate strength of perforated steel plates under combined biaxial compression and edge shear loads. *Thin-Walled Struct.* **2008**, *46*, 207–213. [[CrossRef](#)]
11. Paik, J.K. Ultimate strength of steel plates with a single circular hole under axial compressive loading along short edges. *Ships Offshore Struct.* **2007**, *2*, 355–360. [[CrossRef](#)]
12. Paik, J.K. Ultimate strength of perforated steel plates under edge shear loading. *Thin-Walled Struct.* **2007**, *45*, 301–306. [[CrossRef](#)]
13. Saad-Eldeen, S.; Garbatov, Y.; Guedes Soares, C. Strength assessment of steel plates subjected to compressive load and dent deformation. *Struct. Infrastruct. Eng.* **2016**, *12*, 995–1011. [[CrossRef](#)]
14. Saad-Eldeen, S.; Garbatov, Y.; Soares, C.G. Experimental investigation on the residual strength of thin steel plates with a central elliptic opening and locked cracks. *Ocean Eng.* **2016**, *115*, 19–29. [[CrossRef](#)]
15. Saad-Eldeen, S.; Garbatov, Y.; Soares, C.G. Experimental strength analysis of steel plates with a large circular opening accounting for corrosion degradation and cracks subjected to compressive load along the short edges. *Mar. Struct.* **2016**, *48*, 52–67. [[CrossRef](#)]
16. Saad-Eldeen, S.; Garbatov, Y.; Soares, C.G. Experimental compressive strength analyses of high tensile steel thin-walled stiffened panels with a large lightening opening. *Thin-Walled Struct.* **2017**, *113*, 61–68. [[CrossRef](#)]
17. Saad-Eldeen, S.; Garbatov, Y.; Soares, C.G. Buckling collapse tests of deteriorated steel plates with multiple circular openings. *Ocean Eng.* **2019**, *172*, 523–530. [[CrossRef](#)]
18. Saad-Eldeen, S.; Garbatov, Y.; Soares, C.G. Experimental failure assessment of high tensile stiffened plates with openings. *Eng. Struct.* **2020**, *206*, 110–121. [[CrossRef](#)]
19. Han, X.; Liu, Z.; Xu, X.; Ge, C. Study of Stiffness Calculation Method on Reinforced Concrete Beam Strengthened with CFRP. *Adv. Mater. Res.* **2013**, *744*, 455–458. [[CrossRef](#)]
20. Yang, C.X.; Liu, Z.; Sun, L.P.; Li, J. Finite element analysis of shear behavior of reinforced concrete beam strengthened by high-strength steel wire mesh. *Appl. Mech. Mater.* **2014**, *482*, 15–19. [[CrossRef](#)]
21. Sun, L.P.; Liu, Z.; Yang, C.X.; Zhang, Z.F. Simulating the stiffness of RC beams strengthened by CFRP with secondary load by ANSYS. *Appl. Mech. Mater.* **2014**, *444*, 1062–1066. [[CrossRef](#)]
22. Wang, P.; Wang, X.; Ma, N. Vertical shear buckling capacity of web-posts in castellated steel beams with fillet corner hexagonal web openings. *Eng. Struct.* **2014**, *75*, 315–326. [[CrossRef](#)]
23. Zirakian, T.; Showkati, H. Distortional buckling of castellated beams. *J. Constr. Steel Res.* **2006**, *62*, 863–871. [[CrossRef](#)]
24. Trahair, N.S. Deformations of geometrically imperfect beams. *J. Struct. Div.* **1969**, *95*, 1475–1496. [[CrossRef](#)]
25. Zhao, Y.; Yan, R.; Wang, H. Experimental Studies of Failure Behavior and Strength of H Beams with Stiffened Web Openings under Compression and Bending Loads. *J. Ship Mech.* **2016**, *20*, 315–322.
26. Li, W.; Chen, Y.; Liu, X. Effect of continuous opening of web on the characteristics of long-span frame. *Ship Sci. Technol.* **2022**, *44*, 16–19.
27. Gan, J.; Shan, O.; Wu, W.; Lin, Y. Ultimate strength analysis of typical perforated high web frame structure in cruise ships. *Chin. J. Ship Res.* **2021**, *16*, 181–188. [[CrossRef](#)]
28. Liu, B.; Yao, X.; Lin, Y.; Wu, W.; Soares, C.G. Experimental and numerical analysis of ultimate compressive strength of long-span stiffened panels. *Ocean Eng.* **2021**, *237*, 109633. [[CrossRef](#)]
29. Liu, B.; Gao, L.; Ao, L.; Wu, W. Experimental and numerical analysis of ultimate compressive strength of stiffened panel with openings. *Ocean Eng.* **2021**, *220*, 108453. [[CrossRef](#)]
30. Qiu, Y.; Yan, R.; Wang, N.; Shen, W.; Xu, S.; Li, M.; Qin, K. Stress amplification effect and fatigue strength evaluation of marine thin plate welded structure considering welding deformation: Theoretical and experimental analysis. *Thin-Walled Struct.* **2023**, *188*, 110871. [[CrossRef](#)]
31. Zhou, H.; Zhang, Q.; Yi, B.; Wang, J. Hardness prediction based on microstructure evolution and residual stress evaluation during high tensile thick plate butt welding. *Int. J. Nav. Archit. Ocean. Eng.* **2020**, *12*, 146–156. [[CrossRef](#)]
32. Zhou, H.; Wang, J. Accurate FE Computation for Out-of-plane Welding Distortion Prediction of Fillet Welding with Considering Self-Constraint. *J. Ship Prod. Des.* **2019**, *35*, 317–327. [[CrossRef](#)]
33. Zhou, H.; Wang, J.; Zhang, H.; Liu, J.; Mo, Z. Prediction and mitigation of out-of-plane welding distortion of a typical block in fabrication of a semi-submersible lifting and disassembly platform. *Mar. Struct.* **2021**, *77*, 102964. [[CrossRef](#)]
34. Zhou, H.; Yi, B.; Niu, Y.; Wei, B.; Du, S.; Zhao, H.; Liu, J.; Wang, J. Application of efficient TEP FE computation on accurate fabrication of cylindrical leg structure of jack-up rig. *Ocean Eng.* **2020**, *196*, 106812. [[CrossRef](#)]
35. Wang, J.; Rashed, S.; Murakawa, H. FE Analysis of Buckling Behavior Caused by Welding in Thin Plates of High Tensile Strength Steel. *J. Mater. Eng. Perform.* **2014**, *23*, 4358–4365. [[CrossRef](#)]

36. Ueda, Y.; Murakawa, H.; Ma, N. *Welding Deformation and Residual Stress Prevention*; Elsevier Inc.: Amsterdam, The Netherlands, 2012.
37. Murakawa, H.; Deng, D.; Ma, N. Concept of inherent strain, inherent stress and inherent deformation and inherent force for prediction of welding distortion and residual stress. *JWRI Trans.* **2010**, *39*, 103–105.
38. *GB-T 228.1-2021*; Tensile Testing of Metallic Materials Part 1: Room Temperature Test Method. National Standardization Management Committee: Beijing, China, 2021.
39. Chen, C.; Zhou, H.; Lv, Z.; Ge, X.; Xu, X. Experimental and Numerical Investigation of the Buckling Behavior and Strength of Combined Opening Plate Girders in Passenger Ships. *Metals* **2023**, *13*, 1256. [[CrossRef](#)]

**Disclaimer/Publisher’s Note:** The statements, opinions and data contained in all publications are solely those of the individual author(s) and contributor(s) and not of MDPI and/or the editor(s). MDPI and/or the editor(s) disclaim responsibility for any injury to people or property resulting from any ideas, methods, instructions or products referred to in the content.